

## Supplementary Information

Solvation regulation to mitigate the decomposition of 2,6-dihydroxyanthraquinone in aqueous organic redox flow batteries

Kang Peng<sup>#[a]</sup>, Yuanyuan Li<sup>#[a]</sup>, Gonggen Tang<sup>[a]</sup>, Yahua Liu<sup>[b]</sup>, Zhengjin Yang<sup>\*[a]</sup> and Tongwen Xu<sup>\*[a]</sup>

---

[a] K. Peng, Y.Y. Li, G.G. Tang, Prof. Z.J. Yang, Prof. T.W. Xu  
Department of Applied Chemistry, School of Chemistry and Materials Science, University of Science and Technology of China, Hefei 230026, P.R. China.  
E-mail: [yangzj09@ustc.edu.cn](mailto:yangzj09@ustc.edu.cn), [twxu@ustc.edu.cn](mailto:twxu@ustc.edu.cn)

[b] Y.H. Liu  
School of Chemistry and Chemical Engineering, Hefei University of Technology, Hefei, Anhui 230009, PR China  
<sup>#</sup> These authors contributed equally

## Methods

### Materials

2,6-Dihydroxyanthraquinone (DHAQ, 97%) was purchased from Ark Pham. Potassium ferrocyanide trihydrate ( $K_4Fe(CN)_6 \cdot 3H_2O$ , 99%) was purchased from Energy Chemicals (Shanghai, P.R. China). Deuterium oxide ( $D_2O$ , 99.9 atom% D), tetra-methylammonium chloride (TMACl, >98%), and tetra-ethylammonium chloride (TEACl, >98%) was purchased from Shanghai Aladdin Biochemical Technology Co., Ltd. Lithium hydroxide (LiOH, >99%), sodium hydroxide (NaOH, >99%), and potassium hydroxide (KOH, >99%) were purchased from Sinopharm Chemical Reagent CO. Ltd. (Shanghai, P.R. China). All chemicals were used as received without further purification. Deionized (DI) water was utilized throughout the experiment.

### $^1H$ NMR spectroscopy

Because  $DHAQ^{2-}$  is stable in air, we performed  $^1H$  NMR titration studies of  $DHAQ^{2-}$  and collected 2D  $^1H$  COSY NMR spectrum of  $DHAQ^{2-}$  and  $TMA^+$  directly in air.  $^1H$  NMR titration studies of  $DHAQ^{2-}$  were performed by dissolving 0.1 M DHAQ, 1.0 M KOH and the desired amount of TMACl, TEACl or KCl in 500  $\mu L$  of  $D_2O$ . 2D  $^1H$  COSY NMR sample of  $DHAQ^{2-}$  and  $TMA^+$  was prepared by dissolving 0.1 M DHAQ, 1.0 M TMACl and 1.0 M KOH in 500  $\mu L$  of  $D_2O$ .

$DHAHQ^+$ ,  $DHA^{2-}$  and  $DHAL^{2-}$  anions are oxygen-sensitive. We performed  $^1H$  NMR titration studies of  $DHAHQ^+$  by firstly charging 0.2 M DHAQ in 2.0 M KOH in  $D_2O$  to 0.2 M  $DHAHQ^+$  in a glovebox with oxygen level of < 2 ppm. Then to 250  $\mu L$  of  $DHAHQ^+$  was added the desired amount of TMACl, which was finally diluted to 500  $\mu L$  by  $D_2O$  in air-tight NMR tubes. The sample with 1.0 M TMACl was prepared similarly for 2D  $^1H$  COSY NMR spectrum of  $DHAHQ^+$  and  $TMA^+$ .

$^1H$  NMR spectra for the pristine DHAQ electrolyte and after 100-consecutive galvanostatic cycles were collected by directly diluting 100  $\mu L$  of the electrolyte in 700  $\mu L$  of  $D_2O$  in air-tight NMR tubes in the glovebox. Limited by the access to NMR devices, it took five hours from sample preparation to *ex situ*  $^1H$  NMRs runnings.

$^1H$  NMR samples of the pristine TMACl and TEACl were prepared by dissolving 4.5 M TMACl and 2.5 M TEACl in 1.0 M KOH in 500  $\mu L$  of  $D_2O$ , respectively. All  $^1H$  NMR and 2D  $^1H$  COSY NMR spectra were recorded on AVANCE III HD-600 (600 MHz) spectrometer.

### Raman spectra

Raman spectra were recorded on a LabRamHR Evolution Raman spectrometer using Advantage 785 Raman spectrometer (NanoWizard Ultra Speed & inVia Raman, Germany) equipped with a HeNe laser emitting at 785 nm. The spectral resolution is 5  $cm^{-1}$ . The spectra were collected with an accumulation time of 10 s from a glass tube filled with 400  $\mu L$  electrolyte.

### Cyclic voltammetry (CV) studies

All CV studies were carried out using a ZENNIUM E electrochemical workstation (ZAHNER, Germany), with a glassy carbon (3 mm diameter) working electrode, an Ag/AgCl reference electrode (equilibrated with 3 M NaCl) and a platinum coil counter electrode. The glassy carbon electrode was polished with alumina slurry (0.5  $\mu m$ ) and rinsed with DI  $H_2O$  prior to measurement.

### Molecular dynamics (MD) simulations

MD simulations were carried out using Gromacs package and then visualized with Visual Molecular Dynamics (VMD) software. Partial charges were obtained from Gaussian16 calculations at the M06-2X/6-311G(d,p) level with a Solute Electron Density (SMD) implicit water solvation model, and the other force field parameters were obtained from OPLS\_AA force fields. The TIP3P explicit water model was employed for solvent water molecules. The cutoff radii for vdW and Coulomb interactions were both 15 Å. Particle-mesh Ewald summation method was applied to the long-range Coulomb interactions. For binding energy analysis, both the vdW and Coulomb interactions were calculated using the cutoff method with a cutoff radius of 15 Å. After minimization, each system was run for 10 ns in NPT (isothermal-isobaric) ensemble using a time step of 1 fs, with 5 ns for equilibrium and another 5 ns for data collection. The simulation temperature was 298.15 K and the pressure was 1 bar. Velocity-rescale and Parrinello-Rahman algorithm were used to control the temperature and pressure, respectively.

### Full cell tests

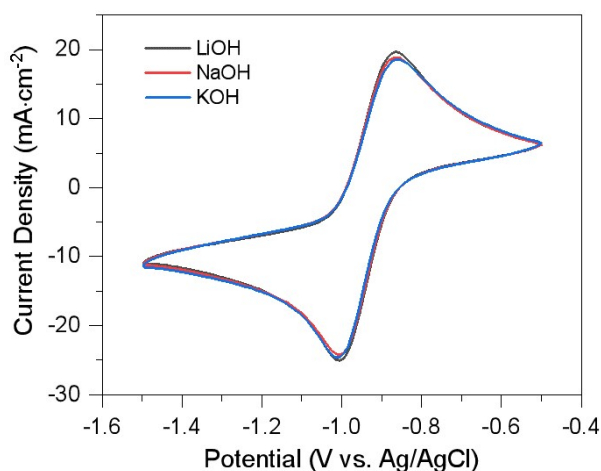
Cell hardware was purchased from Fuel Cell Tech (Albuquerque, US). POCO sealed graphite flow plates with serpentine flow fields were used on both sides. The electrode on each side consisted of 3 stacked sheets of Sigracet SGL 39AA carbon paper electrodes (baked at 400°C for 24 h prior to use) with 5  $cm^2$  geometric area. In all cases, the cell was assembled with a Nafion N117 membrane that had been pretreated by immersion in 1 M KOH aqueous solution for at least 72 hours. The space between the membrane and graphite flow fields was well-sealed with Viton gaskets. The electrolytes were pumped through the cell stack at a flow rate of 60 rpm using a Masterflex L/S peristaltic pump (Cole-Parmer, Vernon Hills, IL). All tubing and electrolyte reservoirs were made from chemically resistant fluorinated ethylene propylene (FEP). Galvanostatic cell cycling was performed in a glovebox with oxygen level of < 2 ppm on a Bio-Logic BCS-815 electrochemical workstation. For the charging process, the cutoff voltage was 1.6 V with a potential hold until the current density fell below 2  $mA\ cm^{-2}$ . For the discharging process, the cutoff voltage was 0.3 V and potential holds were also applied.

For 0.1 M DHAQ/ $K_4Fe(CN)_6$  cell, the negolyte comprised 5 mL of 0.1 M DHAQ, 1.0 M KOH and varied concentrations of TMACl, while the posolyte comprised 30 mL of 0.05 M  $K_4Fe(CN)_6$ , 1.0 M KOH and TMACl of the same concentration. For 0.4 M DHAQ/ $K_4Fe(CN)_6$  cell, the negolyte comprised 5 mL of 0.4 M DHAQ, 1.6 M KOH and 1.0 M of TMACl, while the posolyte comprised 120 mL of 0.05 M  $K_4Fe(CN)_6$ , 1.0 M KOH and 1.0 M TMACl. In each cell, the posolyte was 1.5 times  $e^-$  excess to make sure the negolyte was the capacity limiting side.

**Table S1** Table of calculated ionic volume ( $i_V^C$ ) and ionic surface area ( $i_{s.a}^C$ ) values for various alkylammonium cations.

Cation	M (g·mol <sup>-1</sup> )	Q (C)	$i_V^C$ (Å <sup>3</sup> )	$i_{s.a}^C$ (Å <sup>2</sup> )
TMA <sup>+</sup>	74.1	1	105.2	128.4
TEA <sup>+</sup>	130.3	1	195.4	177.5
TPA <sup>+</sup>	186.4	1	250.4	273.8
TBA <sup>+</sup>	242.5	1	324.0	355.0

For various alkylammonium cations,  $i_V^C$  and  $i_{s.a}^C$  are shown based on the calculations of Laurence J. Hardwick *et al.*<sup>[1]</sup> Abbreviations are as follows: TMA<sup>+</sup>, tetramethylammonium; TEA<sup>+</sup>, tetraethylammonium; TPA<sup>+</sup>, tetrapropylammonium; TBA<sup>+</sup>, tetrabutylammonium.

**Fig. S1** Cyclic voltammograms collected on glassy carbon working electrode for 0.1 M DHAQ dissolved in H<sub>2</sub>O with 1.0 M LiOH, NaOH or KOH as the supporting electrolyte (Li<sup>+</sup>, Na<sup>+</sup> and K<sup>+</sup>) at a potential scanning rate of 100 mV s<sup>-1</sup>.**Table S2** Stokes radius, hydrated radius, and diffusion coefficient of Li<sup>+</sup>, Na<sup>+</sup>, K<sup>+</sup>, NH<sub>4</sub><sup>+</sup> and TMA<sup>+</sup>, respectively, at 25 °C.<sup>[2]</sup>

Cation	Stokes radius (Å)	Hydrated radius (Å)	Diffusion coefficient (10 <sup>-5</sup> cm <sup>2</sup> s <sup>-1</sup> )
Li <sup>+</sup>	2.38	3.82	1.029
Na <sup>+</sup>	1.84	3.58	1.334
K <sup>+</sup>	1.25	3.31	1.957
NH <sub>4</sub> <sup>+</sup>	1.25	3.31	1.957
TMA <sup>+</sup>	2.05	3.67	1.196

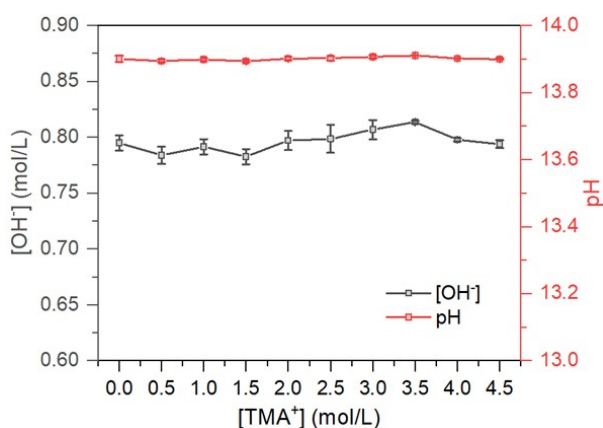


**Fig. S2** Results of three parallel titrations of aqueous solutions of 0.8 M KOH with increasing TMA<sup>+</sup> concentration from 0.5 M to 4.5 M, using bromocresol green-methyl red as the indicator.

Notes: We used the acid-base titration method to study the pH values and the OH<sup>-</sup> concentrations of aqueous solutions of 0.8 M KOH with increasing the concentration of TMA<sup>+</sup> from 0.5 M to 4.5 M, with bromocresol green-methyl red as color indicators. Results of three parallel titrations are shown in **Fig. S2**. The results show that TMA<sup>+</sup> cations barely associate with OH<sup>-</sup> ions to lower the overall pH. In the meantime, the equilibrium redox potential of DHAQ is pH-independent at pH above 11.7, meaning both the oxidized and the reduced forms are fully deprotonated.<sup>[3]</sup>

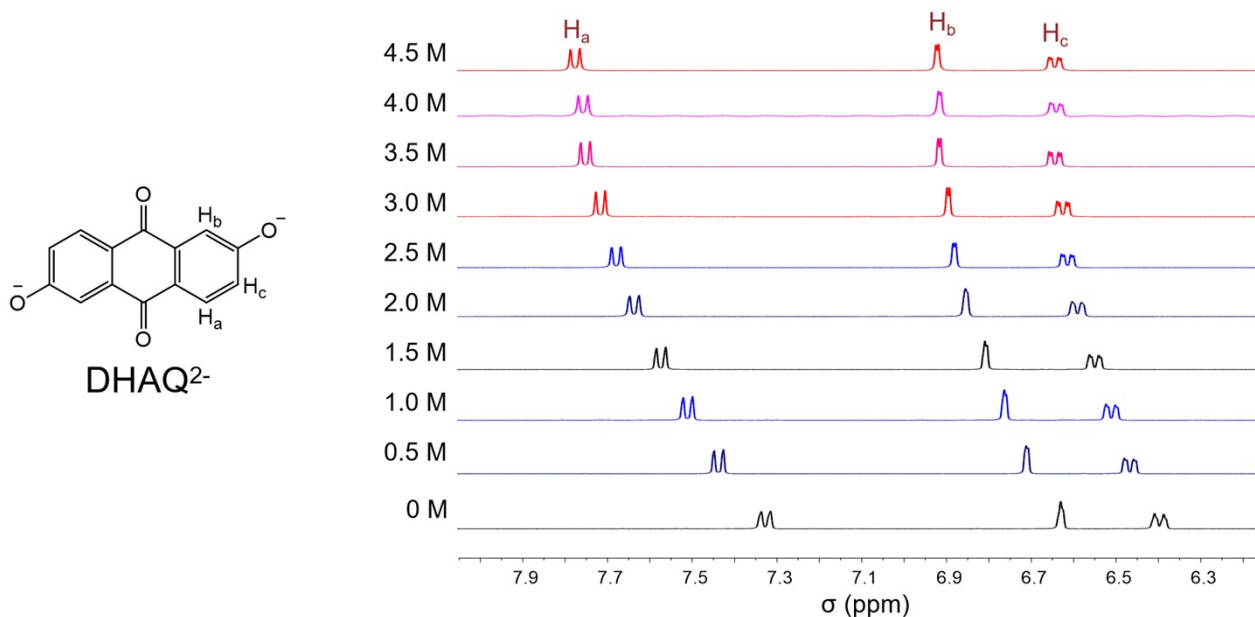


**Fig. S3** <sup>1</sup>H NMR titration of 0.1 M DHAQ<sup>2-</sup> dissolved in 1.0 M KOH in D<sub>2</sub>O with varied concentrations of TMA<sup>+</sup> (from bottom to top are 0, 0.5, 1.0, 1.5, 2.0, 2.5, 3.0, 3.5, 4.0, and 4.5 M in order, respectively).

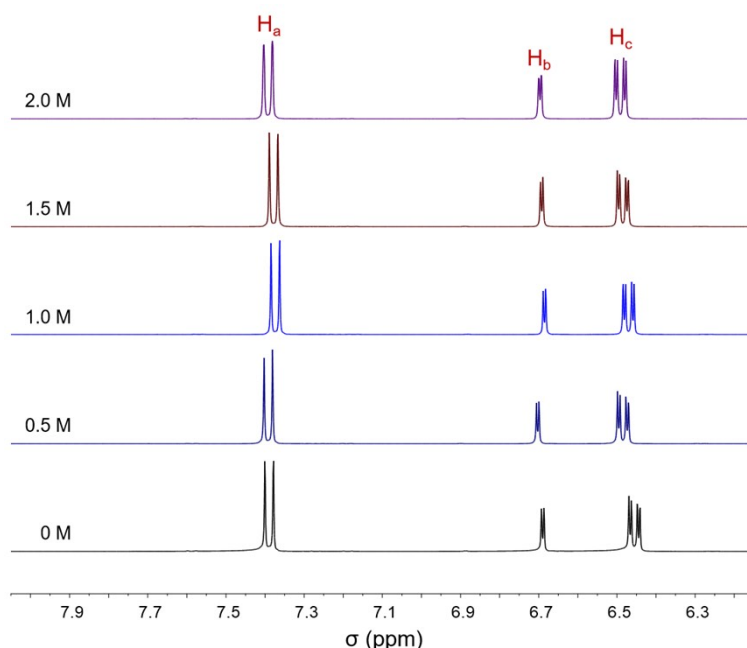


**Fig. S4**  $^1\text{H}$  NMR titration of 0.1 M  $\text{DHAQ}^{2-}$  dissolved in 1.0 M KOH in  $\text{D}_2\text{O}$  with varied concentrations of KCl (from bottom to top are 0, 0.5, 1.0, 1.5, and 2.0 M in order, respectively).

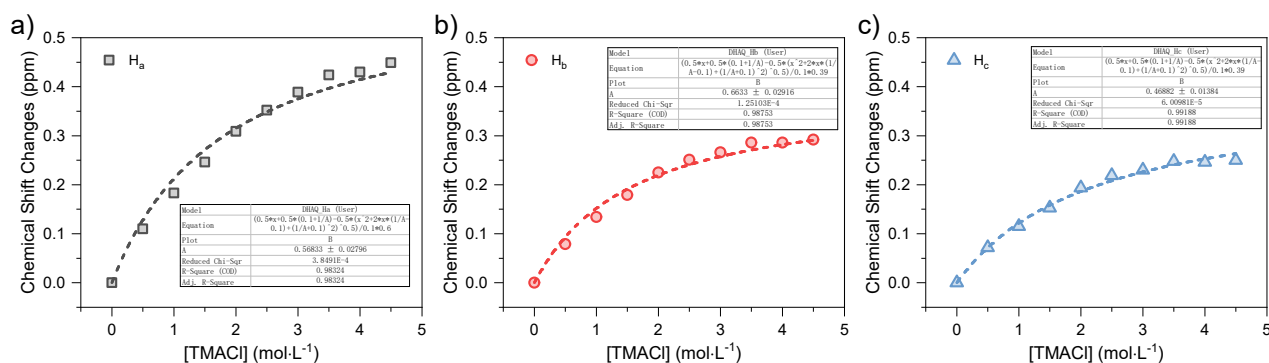


**Fig. S5** Chemical shift changes of (a)  $\text{H}_a$ , (b)  $\text{H}_b$ , and (c)  $\text{H}_c$  on  $\text{DHAQ}^{2-}$  upon addition of  $\text{TMA}^+$ . The fitting curves (dashed lines) are derived from the nonlinear curve-fitting equation<sup>[4]</sup> for measuring supramolecular interactions as follow:

$$\Delta\delta = \frac{0.5[\text{TMA}^+] + 0.5\left([\text{DHAQ}^{2-}] + \frac{1}{K_a}\right) - 0.5\sqrt{[\text{TMA}^+]^2 + 2[\text{TMA}^+]\left(\frac{1}{K_a} - [\text{DHAQ}^{2-}]\right) + \left(\frac{1}{K_a} + [\text{DHAQ}^{2-}]\right)^2}}{[\text{DHAQ}^{2-}]/\Delta\delta_\infty}$$

Where  $K_a$  is the association constant,  $\Delta\delta$  is the chemical shift change of  $\text{H}_a$ ,  $\text{H}_b$  or  $\text{H}_c$  on  $\text{DHAQ}^{2-}$ ,  $\Delta\delta_\infty$  is the chemical shift change of  $\text{H}_a$ ,  $\text{H}_b$  or  $\text{H}_c$  when  $\text{DHAQ}^{2-}$  is completely complexed,  $[\text{DHAQ}^{2-}]$  is the fixed concentration of  $\text{DHAQ}^{2-}$ ,  $[\text{TMA}^+]$  is the varied concentration of  $\text{TMA}^+$ . The equation is generally used for measuring supramolecular interactions. Chemical shift changes of  $\text{H}_a$ ,  $\text{H}_b$  or  $\text{H}_c$  accord well with the fitting results, indicating the suitability of the equation.

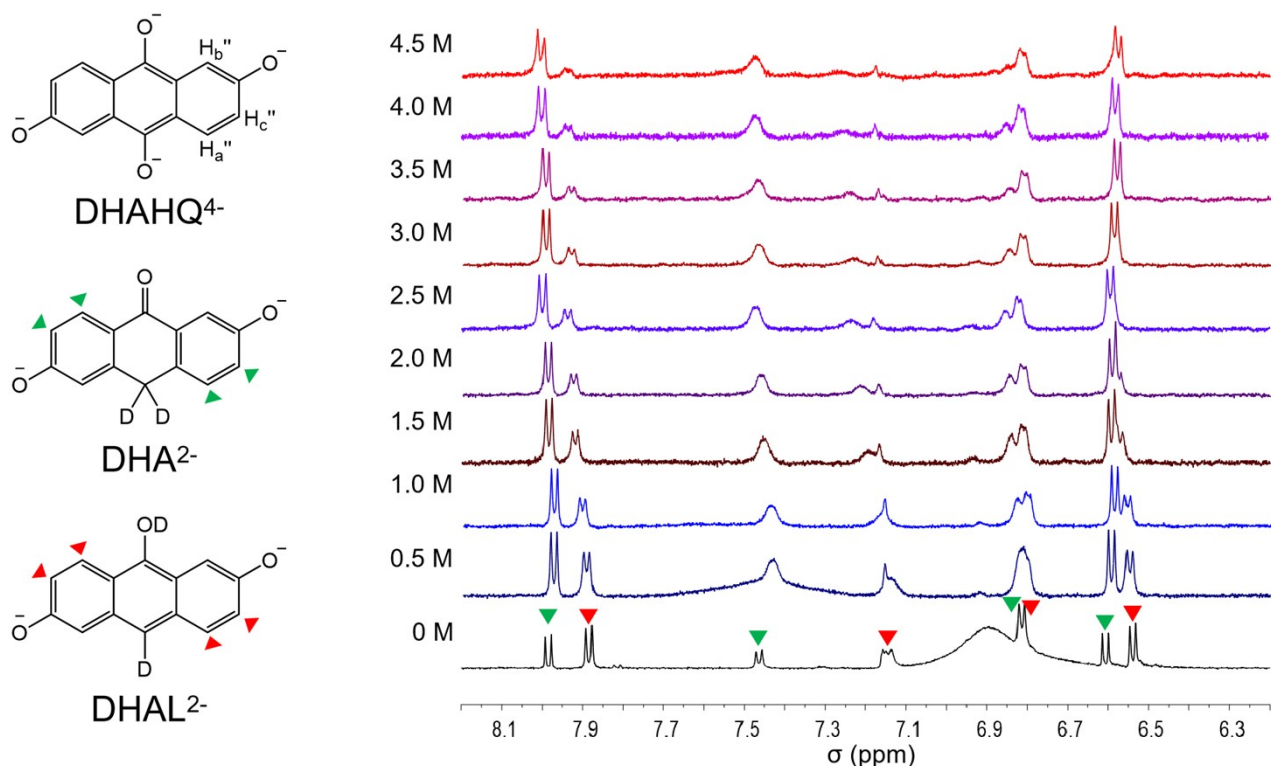


**Fig. S6**  $^1\text{H}$  NMR titration of 0.1 M  $\text{DHAHQ}^{4-}$  dissolved in 1.0 M KOH in  $\text{D}_2\text{O}$  with varied concentrations of  $\text{TMA}^+$  (from bottom to top are 0, 0.5, 1.0, 1.5, 2.0, 2.5, 3.0, 3.5, 4.0, and 4.5 M in order, respectively). It takes five hours from samples preparation to running *ex situ*  $^1\text{H}$  NMRs, with the potential being held.

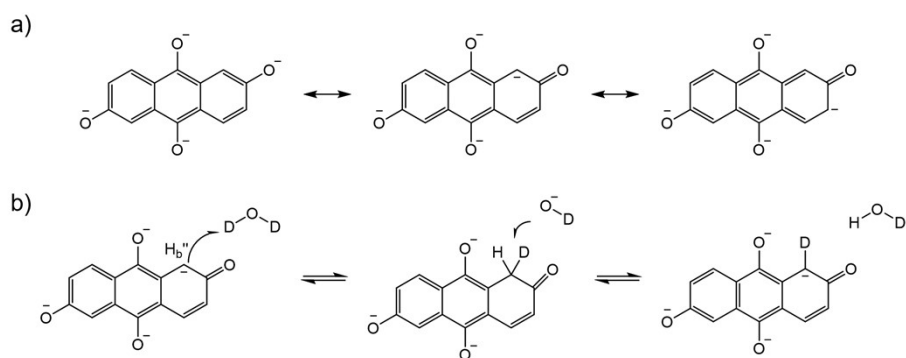


**Fig. S7** (a) Resonance structures of  $\text{DHAHQ}^{4-}$ . (b) Mechanism of the H-D exchange reaction.<sup>[5]</sup>

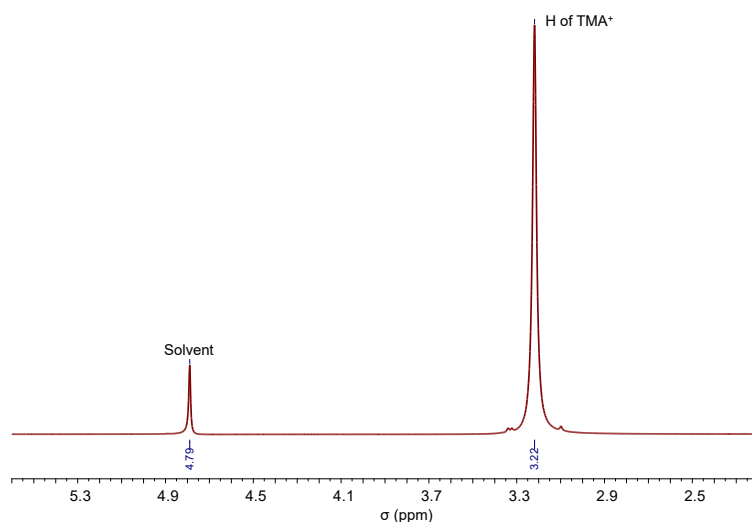


**Fig. S8** The  $^1\text{H}$  NMR spectrum of pristine TMACl.

Notes: We collected the  $^1\text{H}$  NMR spectrum of pristine TMACl to explain its chemical shifts. The H signal of  $\text{TMA}^+$  appears at  $\sim 3.20$  ppm when  $\text{DHAQ}^{2-}$  or  $\text{DHAHQ}^{4-}$  is not present. When it coexists in a solution with  $\text{DHAQ}^{2-}/\text{DHAHQ}^{4-}$ , the electron-donating effect of  $\text{DHAQ}^{2-}/\text{DHAHQ}^{4-}$  cause the H signal of  $\text{TMA}^+$  shift upfield. This effect is related to the concentration of both  $\text{TMA}^+$  and  $\text{DHAQ}^{2-}/\text{DHAHQ}^{4-}$ . For solutions whose major content is  $\text{TMA}^+$  (for instance, at a  $\text{TMA}^+$  concentration of 4.5 M as in our case), no obvious H signal shift will appear. In contrast, for solutions whose major content is  $\text{DHAQ}^{2-}$  or  $\text{DHAHQ}^{4-}$  (in our case, the solution consisting of 0.5 M  $\text{TMA}^+$  and 0.1 M  $\text{DHAQ}^{2-}$ ), obvious upfield shift in H signal will be observed. Thus, the shifts of H signal of  $\text{TMA}^+$  also reveal the ion pairing effect between  $\text{TMA}^+$  and  $\text{DHAQ}^{2-}/\text{DHAHQ}^{4-}$ .

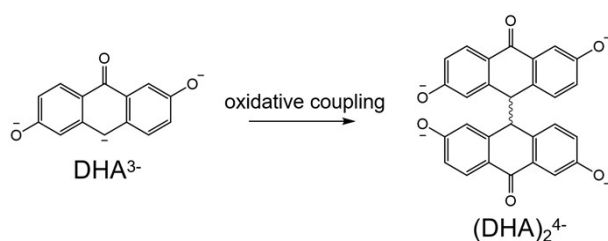


**Fig. S9** The oxidative coupling of DHA carbanions.<sup>[6]</sup>

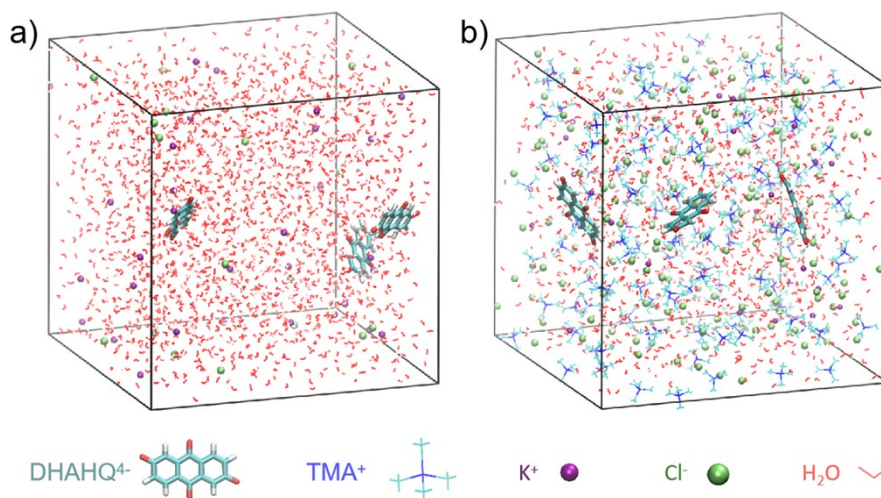


**Fig. S10** Snapshots of the system consisting of (a) 0.1 M  $\text{DHAHQ}^{4-}$  + 1.0 M  $\text{K}^+$  + 4.5 M  $\text{TMA}^+$  and (b) 0.1 M  $\text{DHAHQ}^{4-}$  + 1.0 M  $\text{K}^+$  during MD simulations. In both electrolytes, the solvent is  $\text{H}_2\text{O}$  and the counterion is  $\text{Cl}^-$  (single counterion is used for simplifications).



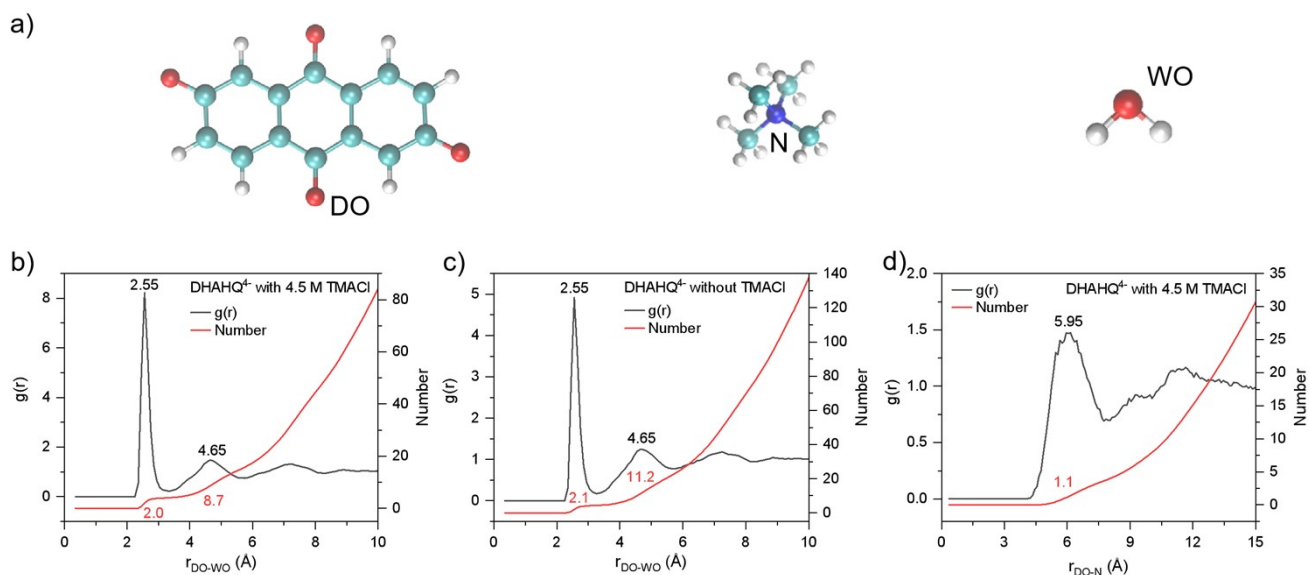


**Fig. S11** (a) Schematic showing O of DHAHQ<sup>4-</sup>, N of TMA<sup>+</sup> and O of H<sub>2</sub>O. The radial distribution functions  $g(r)_{\text{DO-WO}}$  characterizing the distance between O of DHAHQ<sup>4-</sup> and O of H<sub>2</sub>O (a)with and (b)without TMACl. (c) The radial distribution functions  $g(r)_{\text{DO-N}}$  characterizing the distance between O of DHAHQ<sup>4-</sup> and N of TMA<sup>+</sup>.

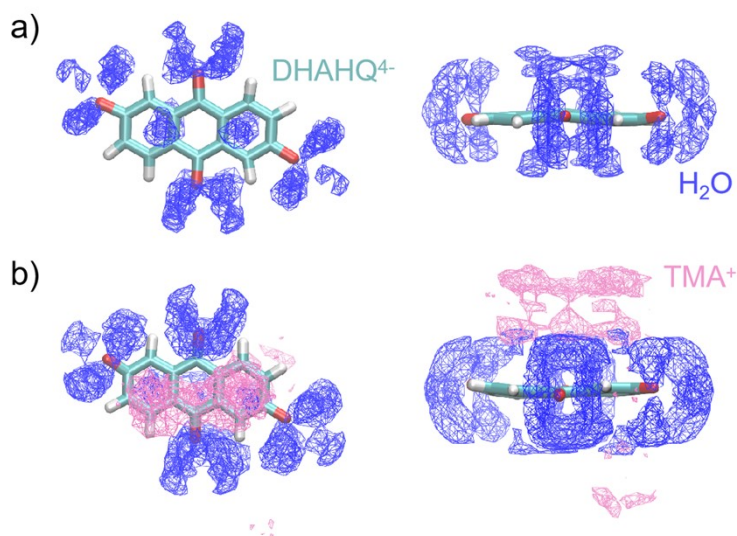


**Fig. S12** Representative aggregates from MD simulations of DHAHQ<sup>4-</sup> and H<sub>2</sub>O (a) without or (b) with TMA<sup>+</sup> from the front and top views. In the middle is the stick model of DHAHQ<sup>4-</sup>, which is surrounded by H<sub>2</sub>O and TMA<sup>+</sup> (the blue and pink represent for their spatial density distributions, respectively).



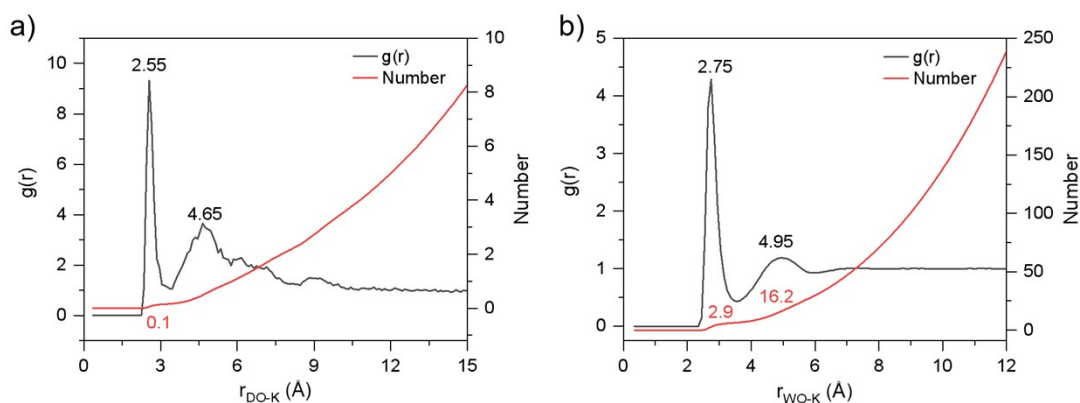


**Fig. S13** The radial distribution functions  $g(r)_{\text{DO-K}}$  and  $g(r)_{\text{WO-K}}$  characterizing the distance between O of DHAHQ<sup>4-</sup> and K<sup>+</sup>, and O of H<sub>2</sub>O and K<sup>+</sup>, respectively.

Notes: We believe the reason why DHAQ<sup>2-</sup> and DHAHQ<sup>4-</sup> are unaffected by K<sup>+</sup> is a strong hydration effect of K<sup>+</sup>. We calculated the radial distribution functions  $g(r)_{\text{DO-K}}$  and  $g(r)_{\text{WO-K}}$  characterizing the distance between O of DHAHQ<sup>4-</sup> and K<sup>+</sup>, and O of H<sub>2</sub>O and K<sup>+</sup>, respectively, as shown in **Fig. S13**. K<sup>+</sup> could hardly enter the primary solvation sheath of DHAHQ<sup>4-</sup>, with an occurrence number of less than 0.1, indicating a negligible possibility. Meanwhile, the primary solvation sheath of K<sup>+</sup> has 2.9 water molecules and the secondary solvation sheath has 16.2 water molecules. Hydrated K<sup>+</sup> is too big and it is very hard for K<sup>+</sup> to shed off the hydration shell and to move towards DHAHQ<sup>4-</sup> thereby altering its hydration structure.

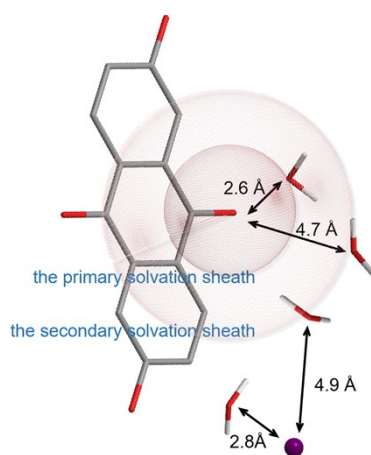


**Fig. S14** The solvation structure of DHAHQ<sup>4-</sup> with K<sup>+</sup>. O, C, H, and K atoms are displayed in red, grey, white, and purple, respectively.

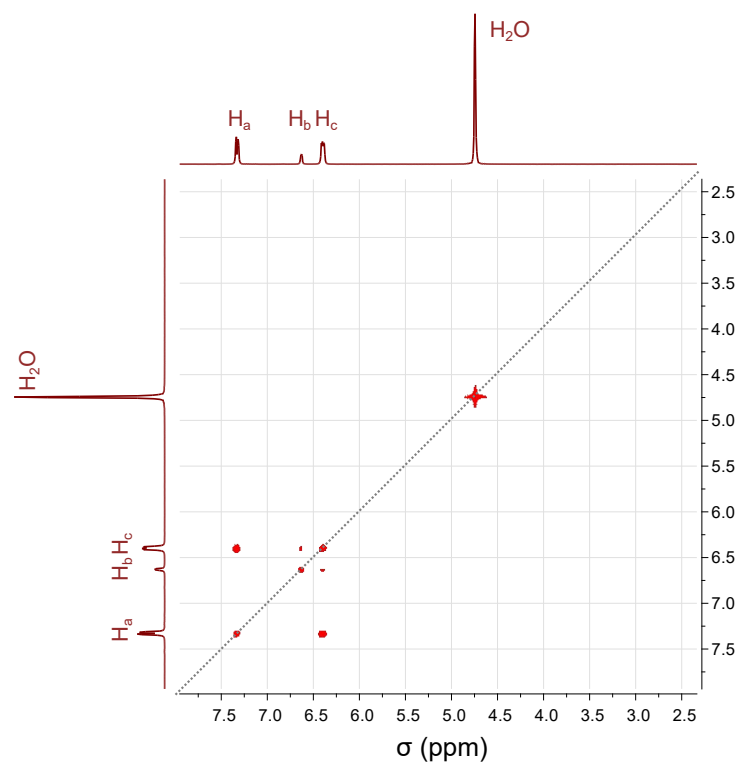


**Fig. S15** 2D NMR (COSY) spectra of 0.1 M DHAQ<sup>2-</sup> dissolved in 1.0 M KOH in D<sub>2</sub>O.

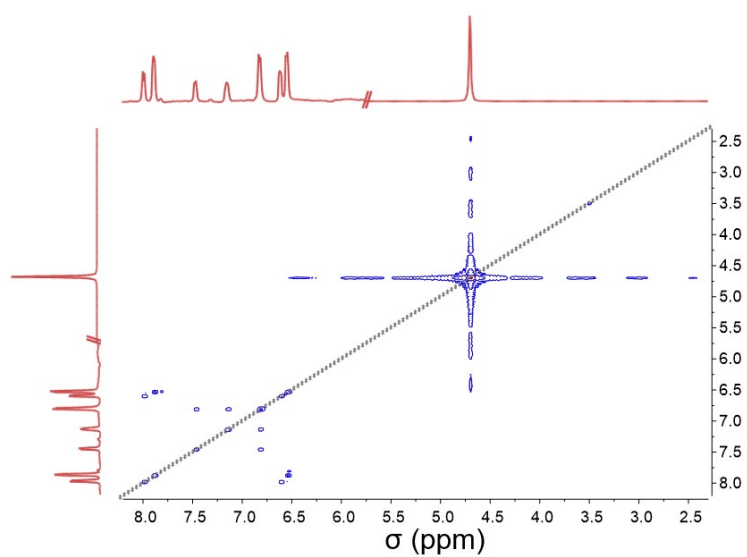


**Fig. S16** 2D NMR (COSY) spectra of 0.1 M DHAHQ<sup>4+</sup> dissolved in 1.0 M KOH in D<sub>2</sub>O.

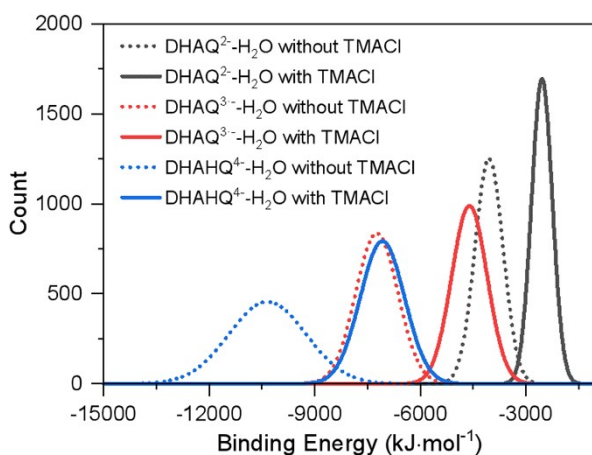


**Fig. S17** Distribution of computed binding energies, i.e., the sum of Coulomb and van der Waals interaction energies, of DHAQ<sup>2-</sup>-H<sub>2</sub>O, DHAQ<sup>3-</sup>-H<sub>2</sub>O, and DHAHQ<sup>4-</sup>-H<sub>2</sub>O with (solid curves) or without (dash curves) TMACI.

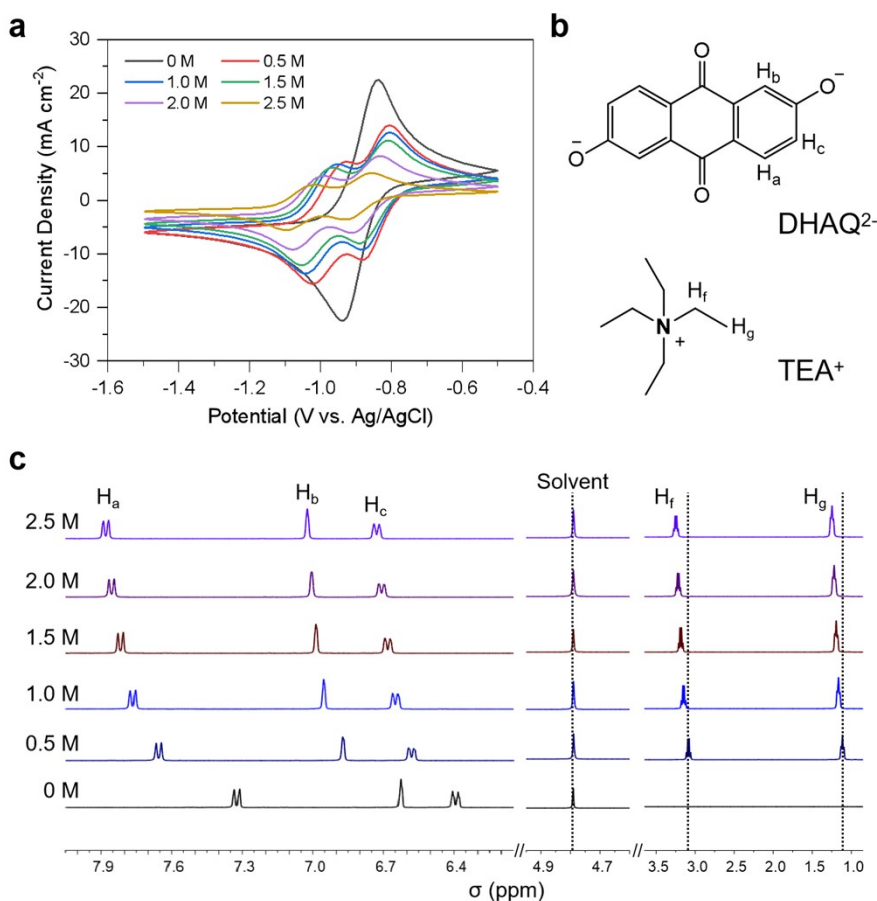


**Fig. S18** (a) Cyclic voltammograms of 0.1 M DHAQ dissolved in 1.0 M KOH aqueous solution with varying concentrations of TEACl. The voltage scanning rate is 100 mV·s<sup>-1</sup>, with glassy carbon as the working electrode. (b) Molecular structures of DHAQ<sup>2-</sup> and TEA<sup>+</sup>. (c) <sup>1</sup>H NMR titration 0.1 M DHAQ<sup>2-</sup> dissolved in 1.0 M KOH in D<sub>2</sub>O with varied concentrations of TEA<sup>+</sup> (from bottom to top are 0, 0.5, 1.0, 1.5, 2.0, and 2.5 M in order, respectively).

Notes: These criteria for selecting supporting electrolyte salts, such as breaking the hydrogen bonding network between redox-active molecules and water, lowering the kinetic energy of redox-active molecules and enlarging their steric hindrance, and having small ionic volumes for fast ion conduction, can be extended to other types of AORFBs. This is based on the following considerations. (1) As water is a weak nucleophile, nucleophilic addition or substitution is one of chemical decomposition mechanisms for redox-active molecules in AORFBs.<sup>[7]</sup> The breakdown of the hydrogen bonding will suppress the intermolecular electron transfer between redox-active molecules and water, thereby mitigating the decomposition reactions.<sup>[8]</sup> (2) Some redox-active molecules (viologen, TEMPO, and ferrocene) are susceptible to decomposition via mechanisms that involve the collision of the same two molecules.<sup>[9]</sup> Lowering the kinetic energy of redox-active molecules and enlarging their steric hindrance will deactivate the decomposition reaction pathway. (3)

For other types of flow batteries, such as all-vanadium redox flow batteries<sup>[10]</sup>, all-iron flow batteries<sup>[11]</sup> and zinc hybrid-flow batteries<sup>[12]</sup>, these criteria for selecting supporting electrolytes are also applicable. For instance, Li *et al.*<sup>[12]</sup> presented a hybrid electrolyte consisting of water, ethylene glycole (EG) and zinc sulfate (ZnSO<sub>4</sub>). The unique solvation interaction of Zn<sup>2+</sup> with EG can effectively enhance the hydrogen bonding between EG and H<sub>2</sub>O and weaken the solvation interaction of Zn<sup>2+</sup> with H<sub>2</sub>O, thus providing reversible Zn/Zn<sup>2+</sup> chemistry at low temperature.

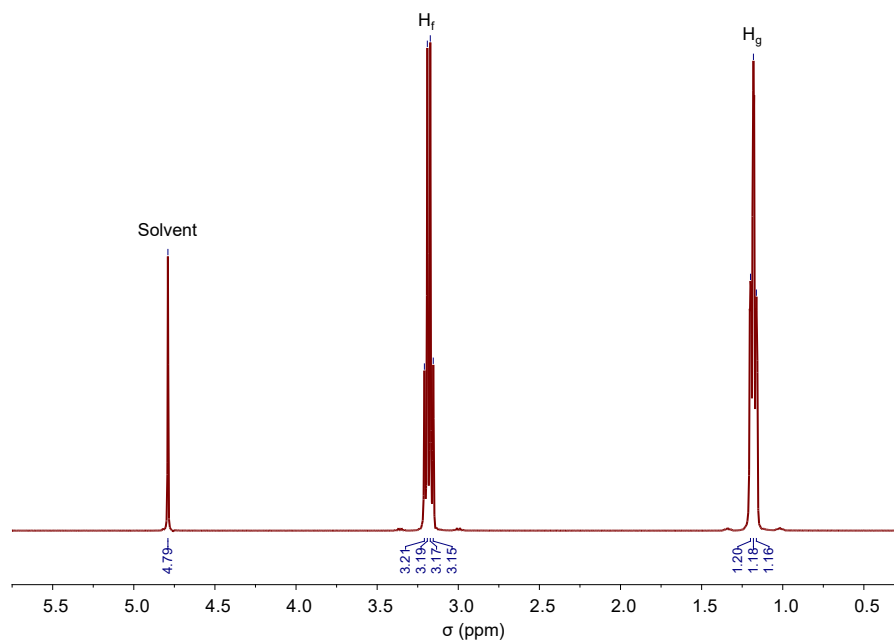


**Fig. S19** The <sup>1</sup>H NMR spectrum of pristine TEACl.

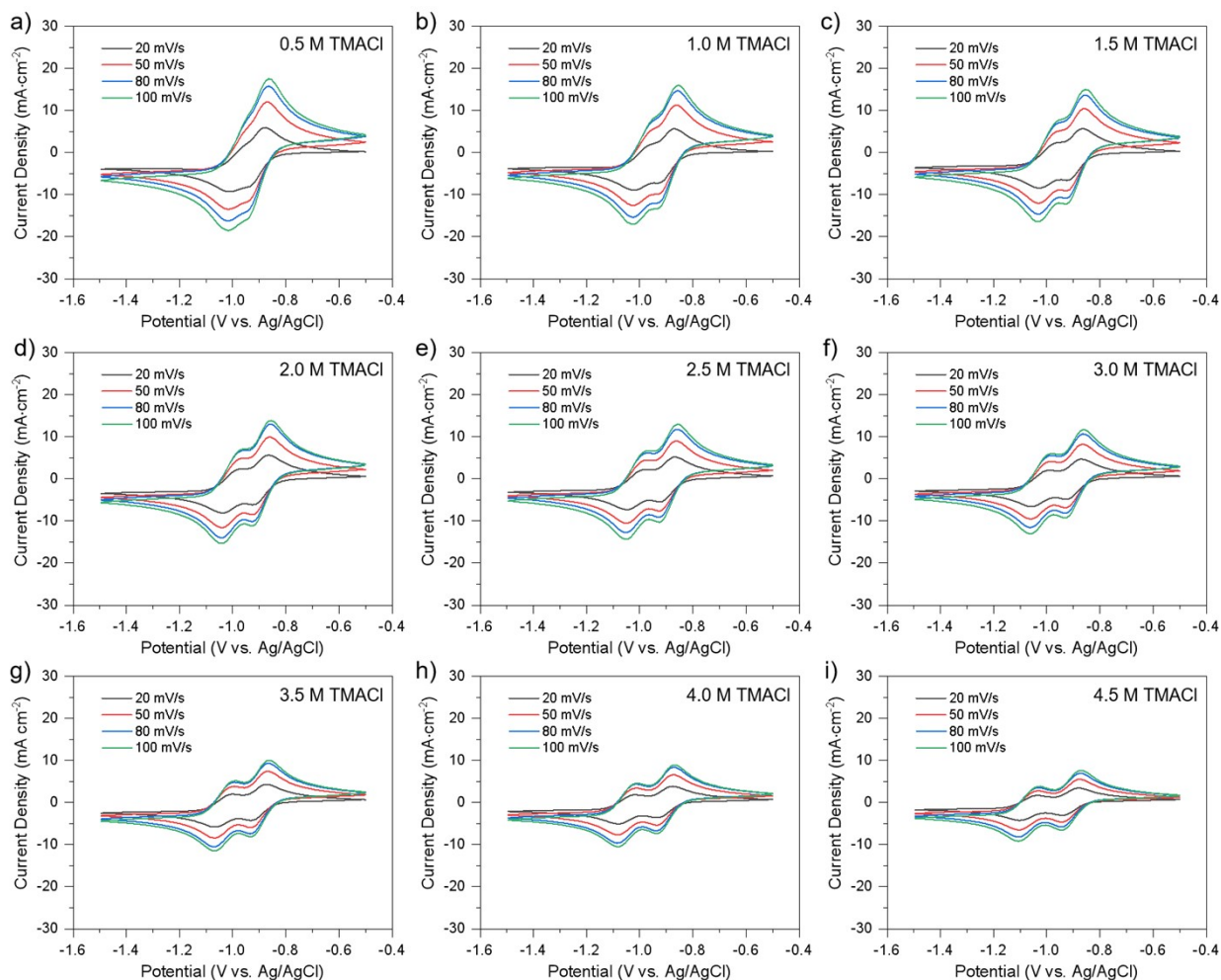
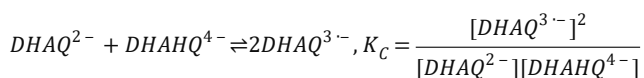
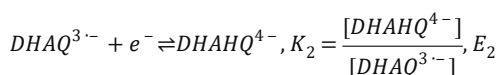
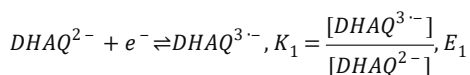


**Fig. S20** Cyclic voltammograms at varied potential scanning rates recorded for 0.1 M DHAQ dissolved in 1.0 M KOH aqueous solution with (a) 0.5 M, (b) 1.0 M, (c) 1.5 M, (d) 2.0 M, (e) 2.5 M, (f) 3.0 M, (g) 3.5 M, (h) 4.0 M, (i) 4.5 M of TMACI, respectively.

According to Grey *et al.*<sup>[5]</sup>, the reduction of DHAQ<sup>2-</sup> in alkaline solutions involves two sequential electron transfer steps and the comproportionation reaction is related to the peak separations ( $E_1$ - $E_2$ ), as shown below.



Considering  $K = \exp\left[\frac{ZF}{RT}(E - E^0)\right]$ , where  $Z$  is the number of transferred electrons and  $E$  is the redox potential, it can be deduced that

$$K_C = \frac{K_1}{K_2} = \exp\left[\frac{ZF}{RT}(E_1 - E_2)\right]$$

Enlarging the peak splitting of the first and the second electron transfer will increase the equilibrium constants of the comproportionation reaction,  $K_C$ , thereby decreasing the concentrations of DHAHQ<sup>4-</sup> at each SOC. This means that in most time, the reduced species is DHAQ<sup>3·-</sup> free radical, which may be more stable than DHAHQ<sup>4-</sup>. This may lead to similar effect as the SOC control strategy does.<sup>[6, 13]</sup>

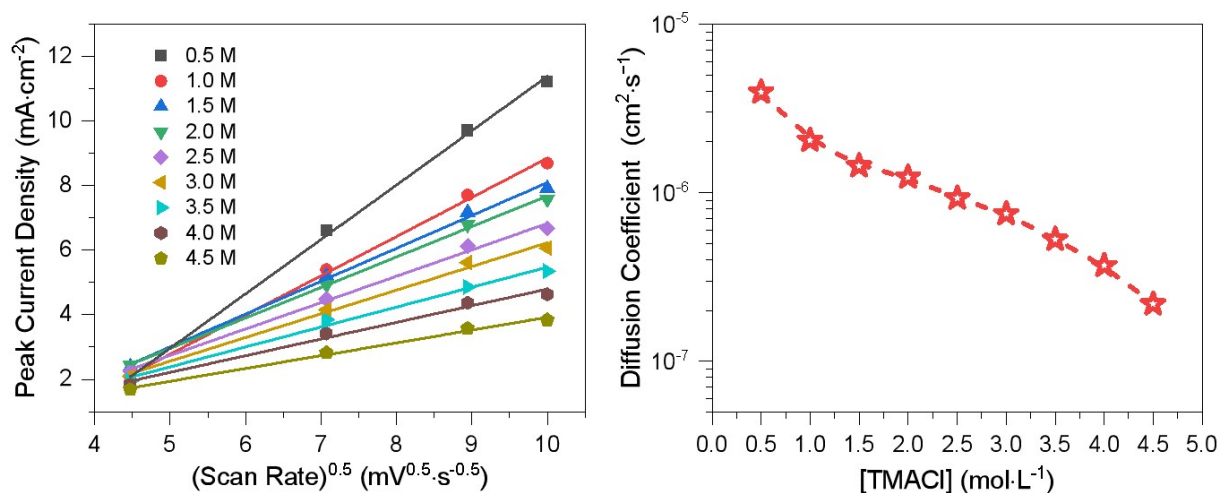


**Fig. S21** (a) Peak current density ( $i_p$ ) versus root of patenting scan rate ( $v^{1/2}$ ) for the oxidation of 0.1 M DHAHQ<sup>4-</sup> in 1.0 M KOH with varied concentrations of TMACl. (b) Effect of the TMA<sup>+</sup> concentration on the diffusion coefficient of DHAHQ<sup>4-</sup>.

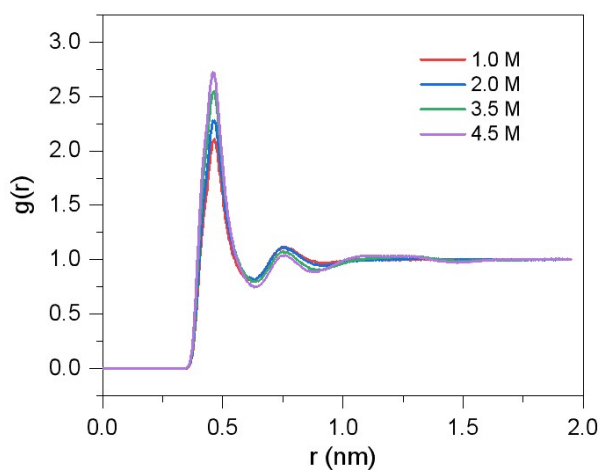


**Fig. S22** Radial distribution functions  $g(r)_{\text{N-O}}$  with respect to distance between N of TMA<sup>+</sup> and O of H<sub>2</sub>O at varied TMA<sup>+</sup> concentrations.

**Table S3** The calculated fraction of free water molecules through MD simulations.

[TMA <sup>+</sup> ] (mol·L <sup>-1</sup> )	0	1.0	2.0	3.5	4.5
Number of TMA <sup>+</sup>	0	30	60	105	135
Total H <sub>2</sub> O number	2056	1867	1635	1359	1161
Number of H <sub>2</sub> O bond with TMA <sup>+</sup>	0	176	344	558	572
Fraction of "free" water (%)	100	90.57	78.96	58.94	50.73

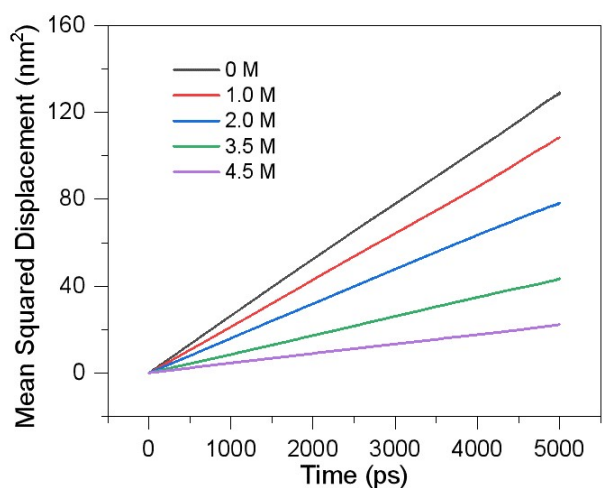


**Fig. S23** The mean-squared displacement (MSD) of H<sub>2</sub>O in the electrolyte as a function of time; the electrolytes have varied concentrations of TMA<sup>+</sup>.

**Table S4** The diffusion rate of H<sub>2</sub>O derived from MSD-time curves as a function of TMA<sup>+</sup> concentration.

[TMACl]	0	1.0	2.0	3.5	4.5
Diffusion Rate (D, ×10 <sup>-5</sup> cm <sup>2</sup> s <sup>-1</sup> )	4.3	3.9	2.6	1.5	0.7

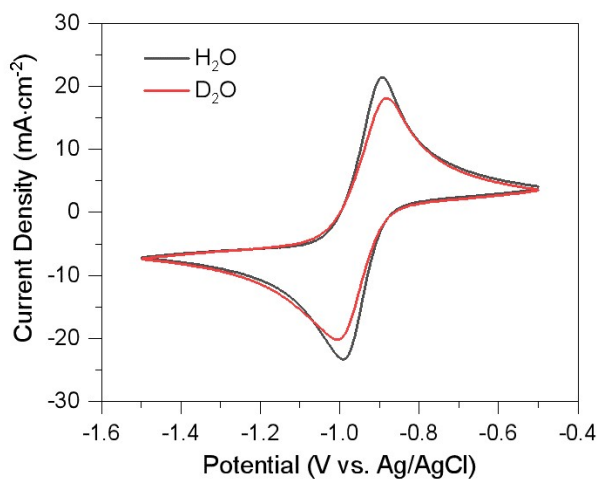


**Fig. S24** Cyclic voltammograms of 0.1 M DHAQ dissolved in H<sub>2</sub>O (blue trace) and D<sub>2</sub>O (red trace) with 1.0 M of KOH as the supporting electrolytes. The potential scanning rate is 100 mV s<sup>-1</sup>, and the experiment was performed on glassy carbon working electrodes.



**Table S5** Electrochemical and physicochemical properties of DHAQ<sup>2-</sup> dissolved in H<sub>2</sub>O and D<sub>2</sub>O with 1.0 M of KOH as the supporting electrolytes, respectively.

Solvent	$E_{1/2}$ (V versus Ag/AgCl)	Peak Separation (mV)	Diffusion Coefficient (D, cm <sup>2</sup> s <sup>-1</sup> )	
			(Red)	(Oxi)
H <sub>2</sub> O	-0.943	98	$6.5 \times 10^{-6}$	$9.9 \times 10^{-6}$
D <sub>2</sub> O	-0.943	120	$4.7 \times 10^{-6}$	$4.9 \times 10^{-6}$

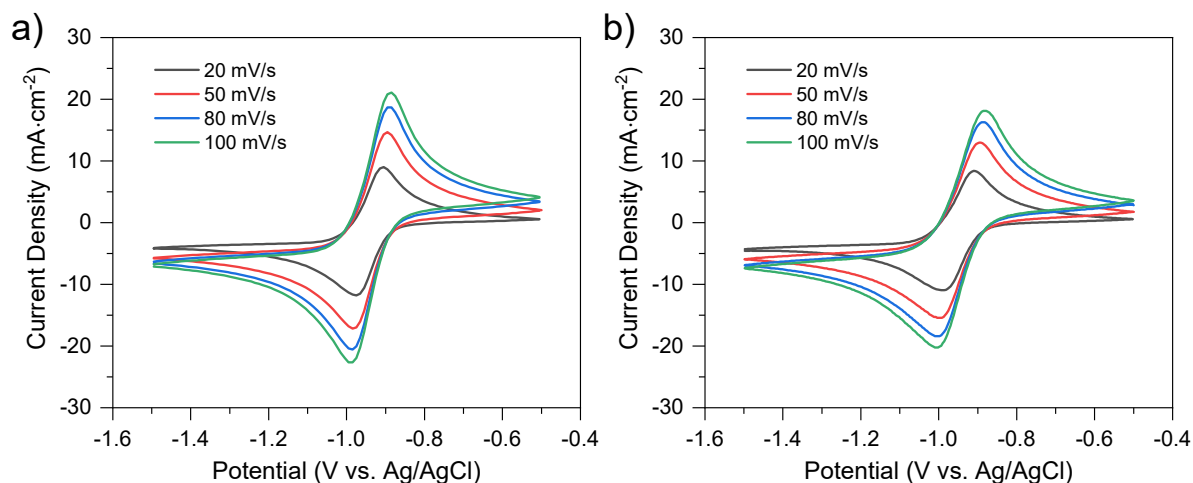


**Fig. S25** Cyclic voltammograms at varied potential scanning rates for 0.1 M DHAQ dissolved in (a) H<sub>2</sub>O and (b) D<sub>2</sub>O, with 1.0 M of KOH as the supporting electrolytes.

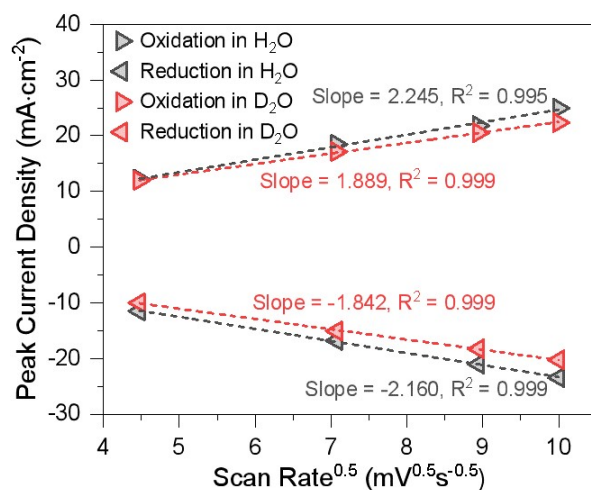


**Fig. S26** Peak current density ( $i_p$ ) versus root of scan rate ( $v^{1/2}$ ) for the redox reaction of 0.1 M DHAQ dissolved in H<sub>2</sub>O and D<sub>2</sub>O with 1.0 M of KOH as the supporting electrolytes, respectively.

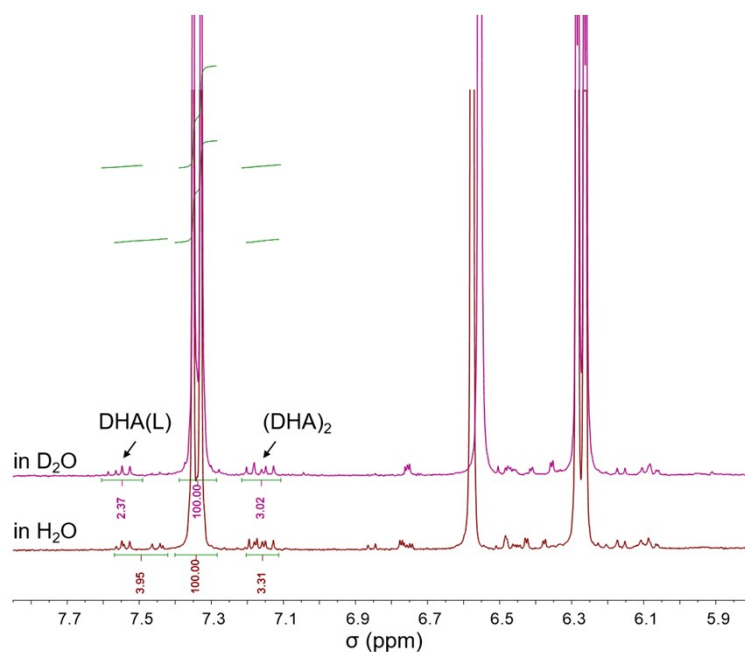


**Fig. S27**  $^1\text{H}$  NMR spectra of cycled DHAQ electrolytes with  $\text{H}_2\text{O}$  and  $\text{D}_2\text{O}$  after 100 cycles, respectively.

Because the DHA signal has one proton, the  $(\text{DHA})_2$  signal has two protons total for each dimer, and the DHAQ signal has two protons. Therefore, the proportion of remaining DHAQ is calculated as shown below.

$$\text{Proportion}_{\text{DHAQ}} = \frac{\text{Integral}_{\text{DHAQ}}/2}{\text{Integral}_{\text{DHA}} + \text{Integral}_{(\text{DHA})_2} + \text{Integral}_{\text{DHAQ}}/2}$$

Where,  $\text{Proportion}_{\text{DHAQ}}$  is the proportion of remaining DHAQ;  $\text{Integral}_{\text{DHA}}$ ,  $\text{Integral}_{(\text{DHA})_2}$  and  $\text{Integral}_{\text{DHAQ}}$  are the peak integral of DHA,  $(\text{DHA})_2$  and DHAQ, respectively. For convenient comparison, we fixed the peak integral of DHA at 100.

Proportions of remaining DHAQ in **Fig. S27** are 90.3% and 87.2%, in consistent with cell cycling experiments in **Fig. 3c**.

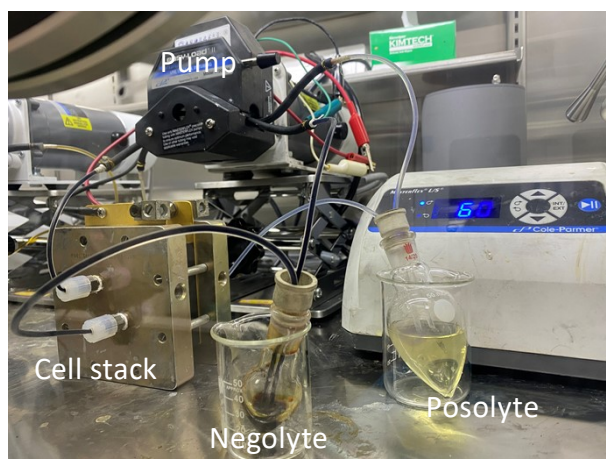


**Fig. S28** Image showing the DHAQ/ $\text{K}_4\text{Fe}(\text{CN})_6$  cell in a glovebox with oxygen level of  $< 2$  ppm.

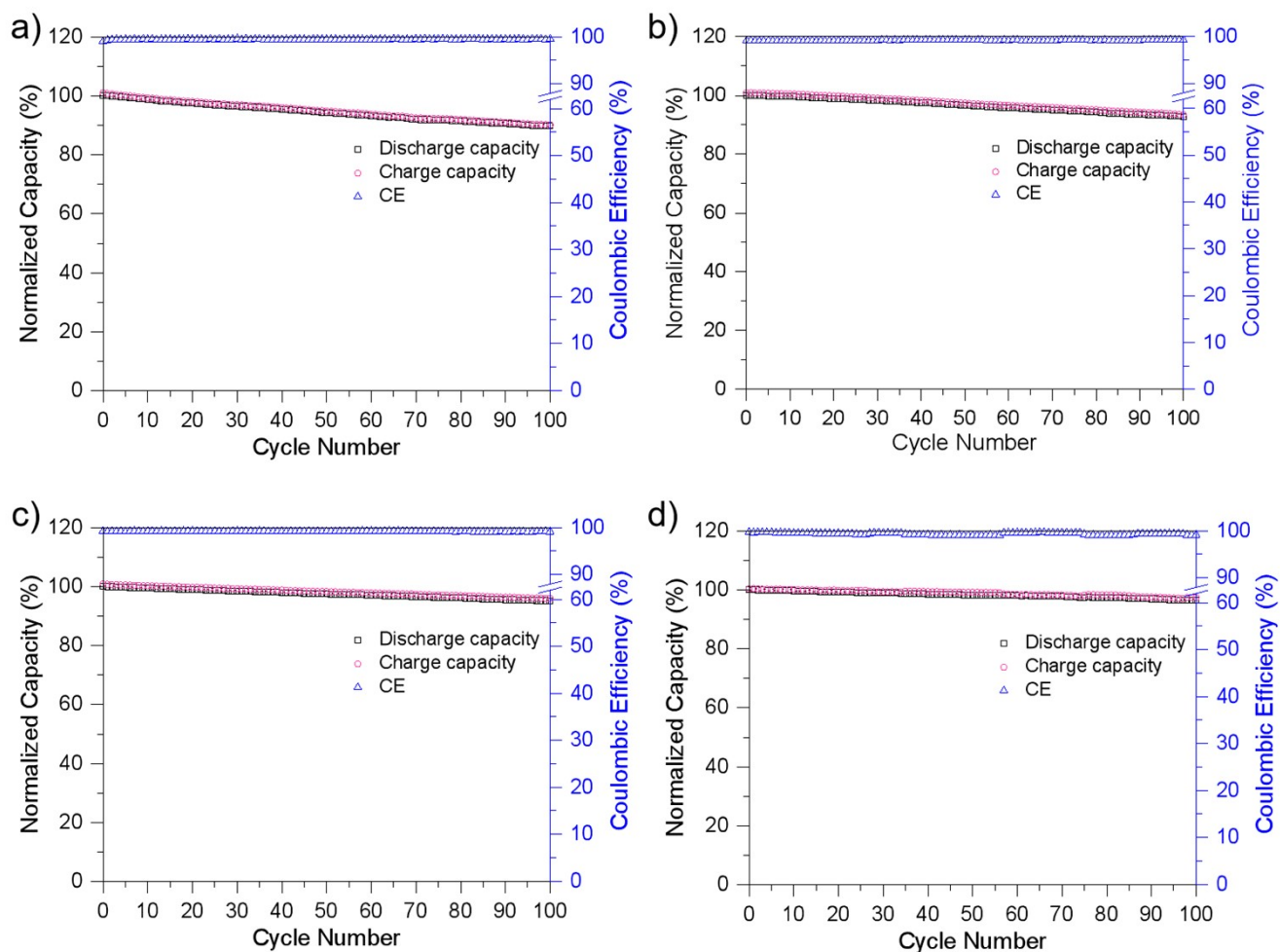


**Fig. S29** Galvanostatic cycling of the DHAQ/K<sub>4</sub>Fe(CN)<sub>6</sub> cells consisted of (a) 1.0 M, (b) 2.0 M, (c) 3.5 M, and (d) 4.5 M of TMACl at 10 mA cm<sup>-2</sup> for 100 consecutive cycles. The normalized charge-discharge capacity and Coulombic efficiency are plotted as functions of the cycle number. The negolyte comprises 5 mL of 0.1 M DHAQ, 1.0 M KOH and varied concentrations of TMACl, while the posolyte comprises 30 mL of 0.05 M K<sub>4</sub>Fe(CN)<sub>6</sub>, 1.0 M KOH and TMACl of the same concentration. The cutoff voltages are 1.6 V and 0.3 V, and a potential hold is applied until the current density falls below 2 mA·cm<sup>-2</sup>.

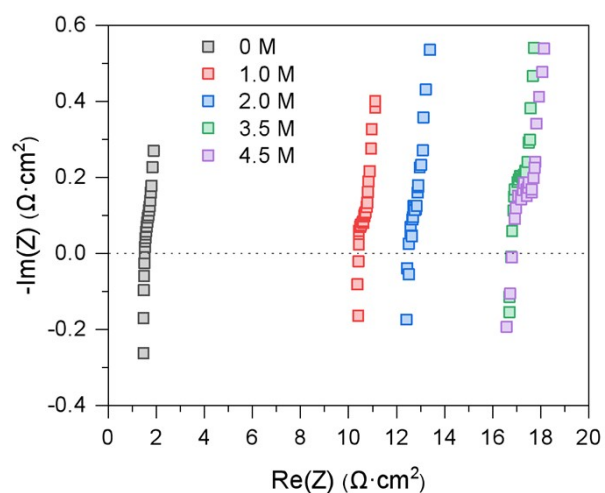


**Fig. S30** High frequency EIS areal specific resistance for 0.1 M DHAQ/ $K_4Fe(CN)_6$  cells with varied concentrations of  $TMA^+$  at ~100% SOC.

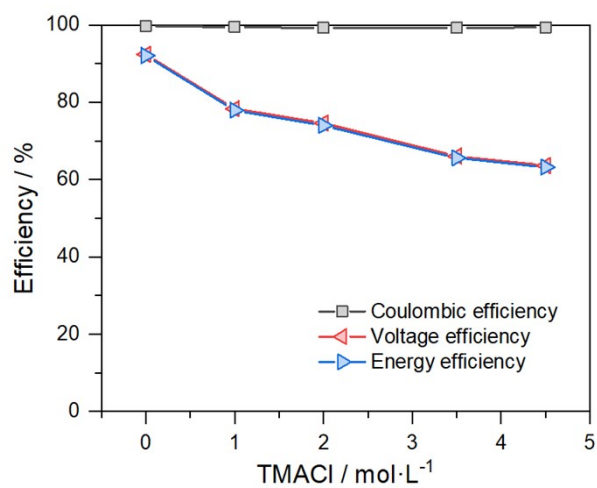


**Fig. S31** The effect of TMACl concentration on the Coulombic efficiency (CE), voltage efficiency (VE) and energy efficiency (EE) of the DHAQ/ $K_4Fe(CN)_6$  cells, derived from Fig. S29.

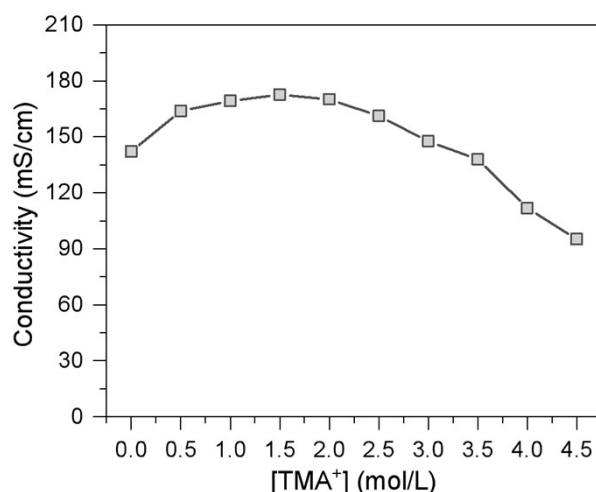


**Fig. S32** The conductivity of electrolytes consisting of 0.1 M DHAQ and 1.0 M KOH with varied TMA<sup>+</sup> concentrations, at 25 °C.

Notes: TMA<sup>+</sup> raises the high-frequency areal-specific resistance of the entire cell (Fig. S30) and we attributed the phenomenon to severe membrane adsorption. Considering that electrolyte resistance also contributes to the whole cell resistance, we measured the conductivity of electrolytes with varied TMA<sup>+</sup> concentrations (Fig. S32). When the concentration of TMA<sup>+</sup> reaches 4.5 M, the conductivity of the solution is still high enough, 95.1 mS/cm (142.1 mS/cm without TMA<sup>+</sup>). Therefore, the increased high-frequency areal-specific resistance is mainly attributed to the increase in membrane resistance. Since the hydrated radius and mobility of TMA<sup>+</sup> cations are comparable to those of inorganic cations (Table S2), it should not be so hard for TMA<sup>+</sup> to migrate across the Nafion 117 membrane. Thus, we believe this is a similar effect as membrane fouling.<sup>[14]</sup> When TMA<sup>+</sup> associates with F atoms of the Nafion 117 membrane, the ion channels may be blocked, thereby increasing membrane resistance. Non-fluorinated cation-exchange membranes may be more compatible.

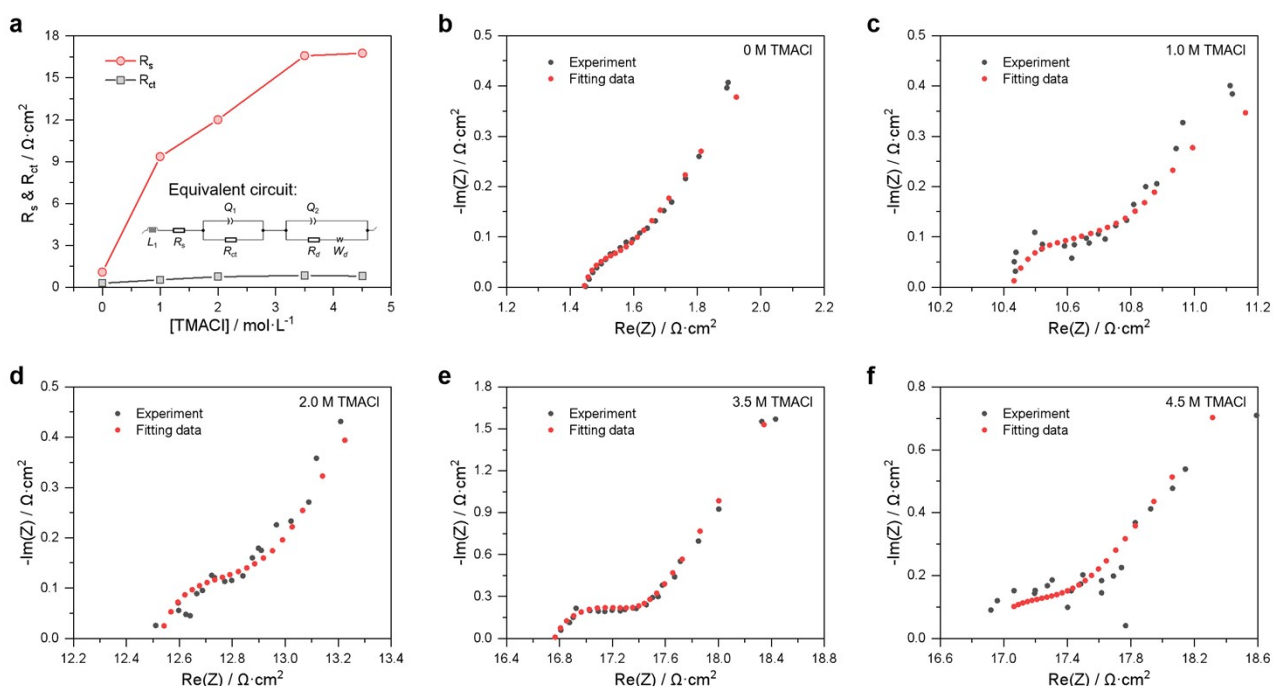


**Fig. S33** (a) The area specific resistance ( $R_s$ ) and electron transfer resistance ( $R_{ct}$ ) derived from the equivalent circuit, which is shown as the inset. (b–f) Experimental and fitted electrochemical impedance spectroscopy (EIS) of the DHAQ/ $K_4Fe(CN)_6$  cells with varied concentrations of TMA<sup>+</sup>.

Notes: According to literature<sup>[15–18]</sup>, electrochemical impedance spectroscopy (EIS) can reveal the battery kinetics. Resistance of the membrane, the electrolyte solution, and the electrodes are dictated by the area specific resistance ( $R_s$ ), and the electron transfer resistance ( $R_{ct}$ ) is directly related to the redox kinetics of the electrolyte. The equivalent circuit used for fitting the experimental data from Fig. S30 is shown as an inset in Fig. S33a, and the details are shown in Figs. S33b–f. With increasing TMA<sup>+</sup> concentrations,  $R_{ct}$  is raised, probably due to the separation of two sequential one-electron transfer steps (Fig. 2h). The increase in  $R_{ct}$  is significantly lower than that in  $R_s$  (Fig. S33a), which is mainly attributed to the increase in membrane resistance (Fig. S32). Non-fluorinated cation-exchange membranes may be more compatible to improve the battery kinetics.

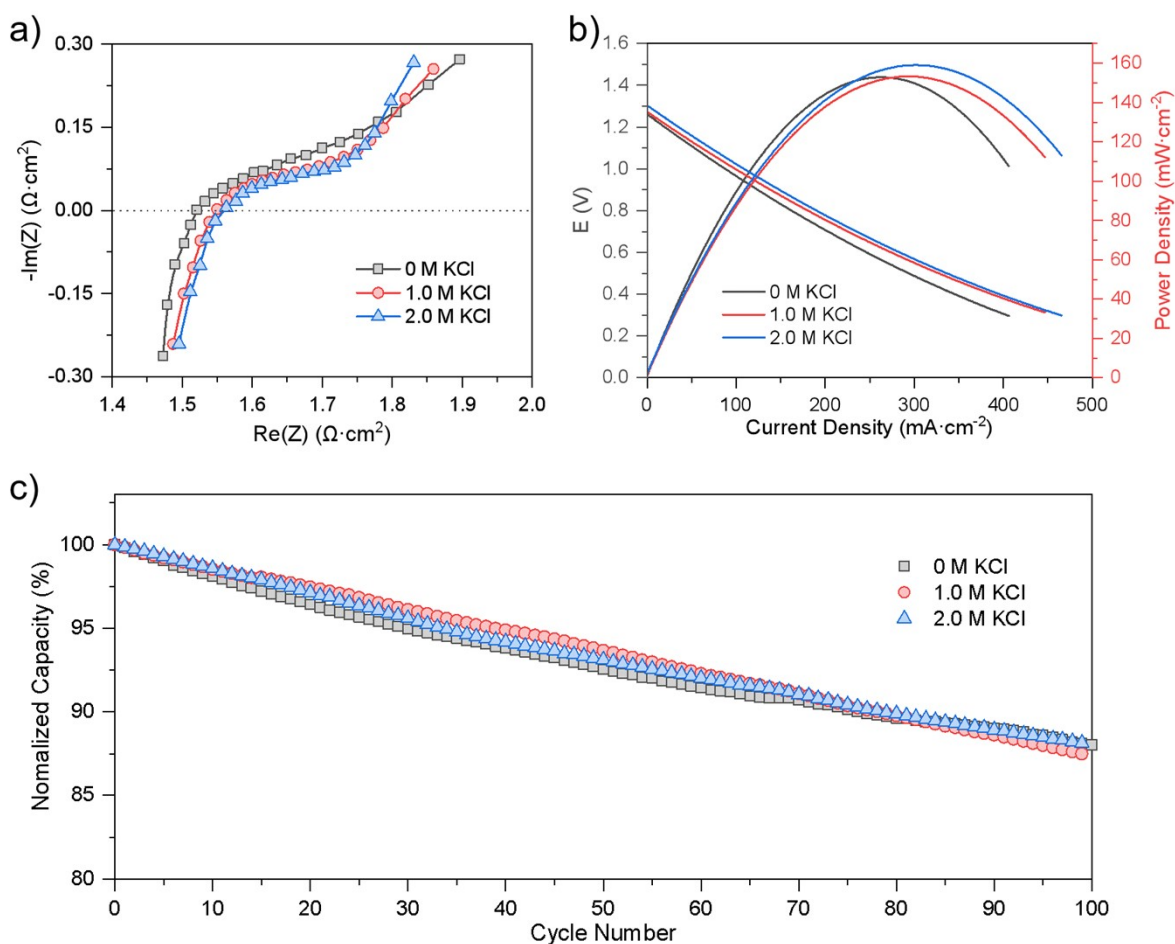


**Fig. S34** The effect of KCl on the cell performance. (a) High frequency EIS areal specific resistance of 0.1 M DHAQ/K<sub>4</sub>Fe(CN)<sub>6</sub> cells at ~100% SOC. (b) Power density and cell voltage of 0.1 M DHAQ/K<sub>4</sub>Fe(CN)<sub>6</sub> cells at ~100% SOC as a function of current density. (c) Galvanostatic cycling of 0.1 M DHAQ/K<sub>4</sub>Fe(CN)<sub>6</sub> cells at 20 mA·cm<sup>-2</sup> with potential cutoffs of 1.6 and 0.3 V, for 100 consecutive cycles. The negolyte comprises 5 mL of 0.1 M DHAQ, 1.0 M KOH and varied concentrations of KCl, while the posolyte comprises 30 mL of 0.05 M K<sub>4</sub>Fe(CN)<sub>6</sub>, 1.0 M KOH and KCl of the same concentration. The potential hold is applied until the current density falls below 2 mA·cm<sup>-2</sup>.

Notes: Galvanostatic cycling of the DHAQ/K<sub>4</sub>Fe(CN)<sub>6</sub> cells at 20 mA·cm<sup>-2</sup> with the addition of 0, 1.0, and 2.0 M KCl were conducted. We did not further raise the concentration of KCl is because when the concentration of KCl is higher than 2.0 M, DHAQ will salt-out. The cell cycling results are shown in **Fig. S34**. It can be seen that the addition of KCl and the increase in its concentration do not affect the cell performance.

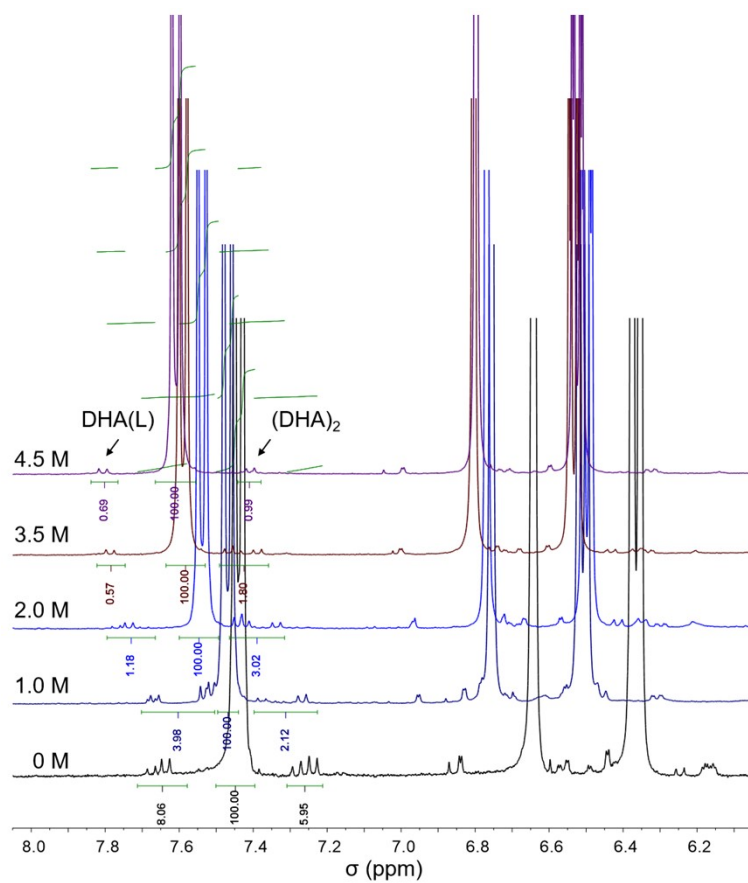


**Fig. S35** <sup>1</sup>H NMR spectra of cycled DHAQ electrolytes in **Fig. 4a**.

Notes: The calculation formula of proportions of remaining DHAQ is same as that in **Fig. S27**. Proportions of remaining DHAQ in **Fig. S35** are 78.1%, 89.1%, 92.3%, 95.5%, and 96.8%, in consistent with cell cycling experiments in **Fig. 4a**.



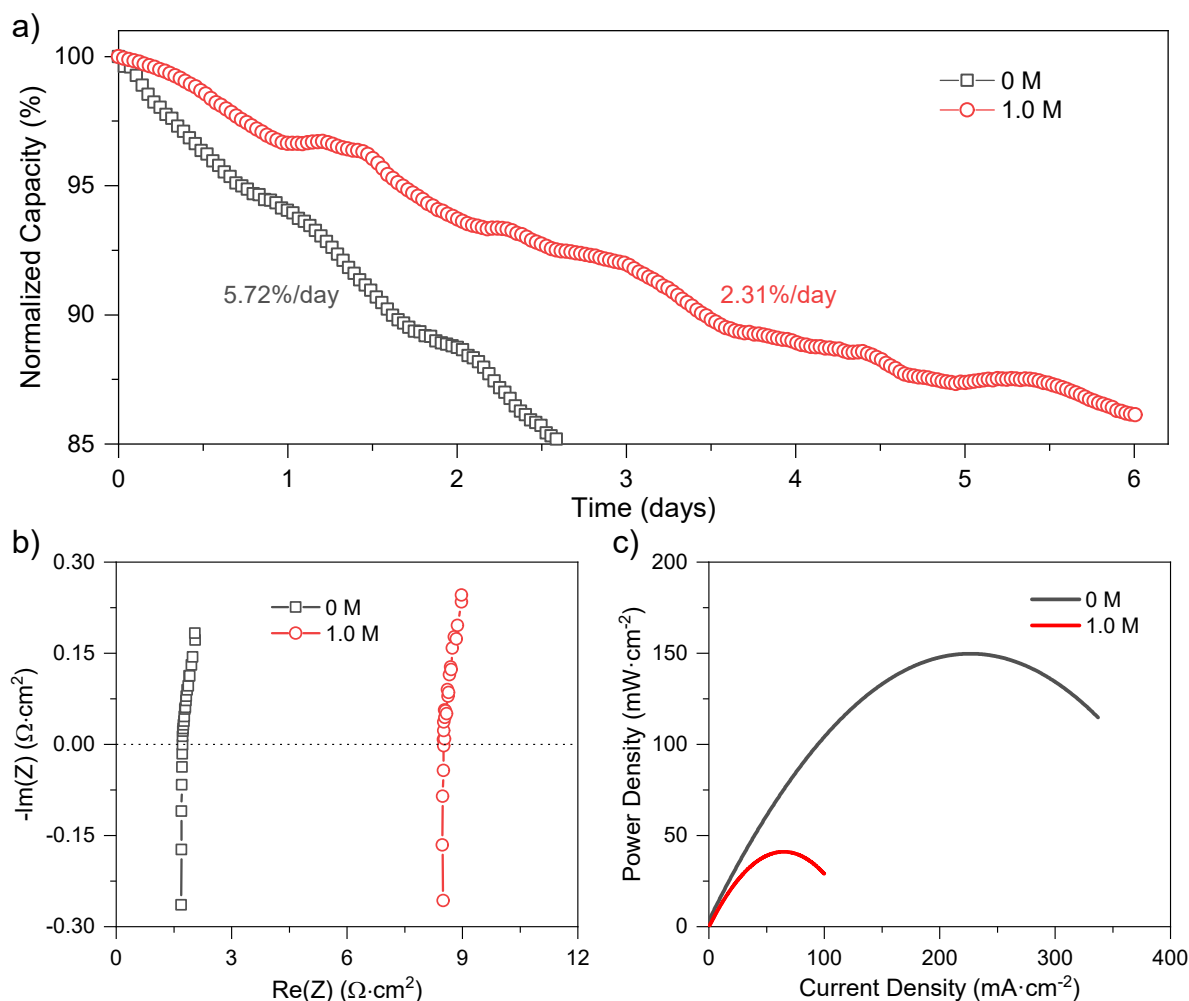


**Fig. S36** (a) Galvanostatic cycling of the 0.4 M DHAQ/ $\text{K}_4\text{Fe}(\text{CN})_6$  cells with 1.0 M TMACI or without TMACI, at  $40 \text{ mA} \cdot \text{cm}^{-2}$ . The normalized discharge capacity is plotted as a function of time. (b) EIS spectra of the DHAQ/ $\text{K}_4\text{Fe}(\text{CN})_6$  cells at 50% SOC, with 1.0 M TMACI or without TMACI. (c) Power density of the DHAQ/ $\text{K}_4\text{Fe}(\text{CN})_6$  cells at  $\sim 100\%$  SOC, with 1.0 M TMACI or without TMACI, as a function of current density. The negolyte comprises 5 mL of 0.4 M DHAQ, 1.6 M KOH and 1.0 M TMACI, while the posolyte comprises 120 mL of 0.05 M  $\text{K}_4\text{Fe}(\text{CN})_6$ , 1.0 M KOH and 1.0 M TMACI. The cutoff voltages are 1.6 V and 0.3 V, and a potential hold is applied until the current density falls below  $2 \text{ mA} \cdot \text{cm}^{-2}$ .

Notes: According to literature<sup>[19,20]</sup> the collision theory is applicable to diffusion-controlled reactions in condensed phases, not only in  $k_D = \frac{4\pi D Z_A Z_B r_c}{\exp(Z_A Z_B r_c / R_c) - 1}$ -controlled rate constant  $k_D$  in condensed phases is derived as below.

$$D = D_A + D_B$$

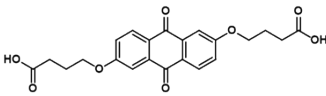
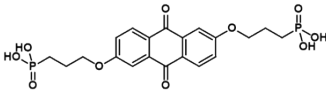
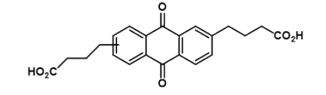
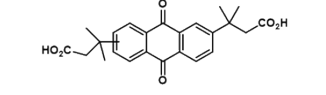
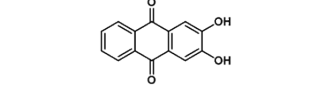
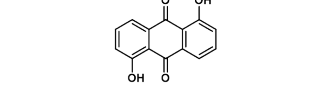
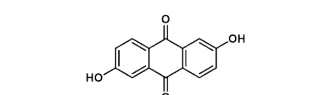
Where  $D_A$  and  $D_B$  are the diffusion coefficients of reactants A and B.  $Z_A$  and  $Z_B$  are the charge numbers of A and B.  $-Z_A Z_B r_c$  is the ionic reaction radius and  $r_c$  is a constant of  $7.1 \times 10^{-8} \text{ cm}$  in water at  $25^\circ \text{C}$ , and  $R_c$  is the radius of the reaction sphere.

In the meantime, some other redox-active species (viologen, TEMPO, and ferrocene) are susceptible to decomposition via mechanisms that involve the collision of the same two molecules in a second-order process.<sup>[9]</sup> Therefore, their decomposition  $r = -\frac{dC_A}{dt} = k_D C_A^2$  be derived as shown below.

Where  $C_A$  is the concentration of the reactant A.

Based on the above analysis, the collision theory may be broadly applicable, and our kinetic regulation strategy can be extended to some other redox-active species in aqueous organic redox flow batteries.

**Table S6** The cycling stability of anthraquinone derivatives based on previous strategies and the proposed solvation regulation strategy.

Strategy		Structure	pH	Demonstrated concentration	Capacity fade (% per day)	Ref.	
Rational molecular engineering	2,6-DBEAQ		12	0.5 M	0.05	[21]	
	2,6-DPPEAQ		9	0.5 M	0.014	[22]	
	DBAQ		12	0.5 M	0.0084	[23]	
	DPivOHAQ		12	0.5 M	0.014		
				14	0.5 M	0.0018	
		2,3-DHAQ		~14	0.2 M	0.8	[24]
	1,5-DHAQ		13.9	0.1 M	0.02	[8]	
SOC control	1.25 V		14	0.1 M	0.14	[6]	
	Deep-discharge		14	0.5 M	0.39	[25]	
Solvation regulation	TMACl			13.9	0.1 M	0.65	This work

Notes: The reported strategies include rational molecular engineering, SOC control. Although tedious synthetic steps and multi-step purifications are required, rational molecular engineering is still the most effective strategy, because it increases the intrinsic stability of chemical structures. SOC control can decrease the quantity of vulnerable species that initiate the subsequent side reactions, or electrochemically recombine redox-active molecules. The proposed solvation regulation strategy is based on altering the kinetic mechanism and the surrounding environment of redox-active molecules. For future improvements, a deep understanding of redox reaction mechanism and decomposition pathways is a prerequisite, and the combination of multiple strategies can be taken into consideration.

## Reference

- [1] P. M. Radjenovic and L. J. Hardwick, *PCCP*, 2019, **21**, 1552-1563.
- [2] E. R. Nightingale, *J. Phys. Chem.*, 1959, **63**, 1381-1387.
- [3] K. Lin, Q. Chen, M. R. Gerhardt, L. Tong, S. B. Kim, L. Eisenach, A. W. Valle, D. Hardee, R. G. Gordon and M. J. Aziz, *Science*, 2015, **349**, 1529-1532.
- [4] Q. Liu, K. Xiao, L. Wen, H. Lu, Y. Liu, X.-Y. Kong, G. Xie, Z. Zhang, Z. Bo and L. Jiang, *J. Am. Chem. Soc.*, 2015, **137**, 11976-11983.
- [5] E. W. Zhao, T. Liu, E. Jónsson, J. Lee, I. Temprano, R. B. Jethwa, A. Wang, H. Smith, J. Carretero-González, Q. Song and C. P. Grey, *Nature*, 2020, **579**, 224-228.
- [6] M.-A. Goulet, L. Tong, D. A. Pollack, D. P. Tabor, S. A. Odom, A. Aspuru-Guzik, E. E. Kwan, R. G. Gordon and M. J. Aziz, *J. Am. Chem. Soc.*, 2019, **141**, 8014-8019.
- [7] D. G. Kwabi, Y. Ji and M. J. Aziz, *Chem. Rev.*, 2020, **120**, 6467-6489.
- [8] S. Huang, H. Zhang, M. Salla, J. Zhuang, Y. Zhi, X. Wang and Q. Wang, *Nat. Commun.*, 2022, **13**, 4746.
- [9] E. S. Beh, D. De Porcellinis, R. L. Gracia, K. T. Xia, R. G. Gordon and M. J. Aziz, *ACS Energy Lett.*, 2017, **2**, 639-644.
- [10] V. Murugesan, Z. Nie, X. Zhang, P. Gao, Z. Zhu, Q. Huang, L. Yan, D. Reed and W. Wang, *Cell Rep. Phys. Sci.*, 2021, **2**, 100323.
- [11] Y. Song, H. Yan, H. Hao, Z. Liu, C. Yan and A. Tang, *Small*, 2022, *n/a*, 2204356.
- [12] N. Chang, T. Li, R. Li, S. Wang, Y. Yin, H. Zhang and X. Li, *Energy Environ. Sci.*, 2020, **13**, 3527-3535.
- [13] M. Wu, M. Bahari, Y. Jing, K. Amini, E. M. Fell, T. Y. George, R. G. Gordon and M. J. Aziz, *Batteries & Supercaps*, 2022, **5**, e202200009.
- [14] M. Gao, M. Salla, F. Zhang, Y. Zhi and Q. Wang, *J. Power Sources* 2022, **527**, 231180.
- [15] P. Sun, Y. Liu, Y. Li, M. A. Shehzad, Y. Liu, P. Zuo, Q. Chen, Z. Yang and T. Xu, *Ind. Eng. Chem. Res.*, 2019, **58**, 3994-3999;
- [16] H. Yang, T. Xiong, Z. Zhu, R. Xiao, X. Yao, Y. Huang and M. S. Balogun, *Carbon Energy*, 2022, **4**, 820-832.
- [17] S. Zhou, P. Huang, T. Xiong, F. Yang, H. Yang, Y. Huang, D. Li, J. Deng and M. S. Balogun, *Small*, 2021, **17**, 2100778.
- [18] Y. Huang, H. Yang, T. Xiong, D. Adekoya, W. Qiu, Z. Wang, S. Zhang and M. S. Balogun, *Energy Storage Mater.*, 2020, **25**, 41-51.
- [19] S. H. Lin, K. P. Li and H. Eyring, in *Reaction in Condensed Phases* (Ed.: H. Eyring), Academic Press, 1975, pp. 1-56;
- [20] R. A. Marcus, *Rev. Mod. Phys.*, 1993, **65**, 599-610.
- [21] D. G. Kwabi, K. Lin, Y. Ji, E. F. Kerr, M.-A. Goulet, D. De Porcellinis, D. P. Tabor, D. A. Pollack, A. Aspuru-Guzik, R. G. Gordon and M. J. Aziz, *Joule*, 2018, **2**, 1894-1906.
- [22] Y. Ji, M.-A. Goulet, D. A. Pollack, D. G. Kwabi, S. Jin, D. De Porcellinis, E. F. Kerr, R. G. Gordon and M. J. Aziz, *Adv. Energy Mater.*, 2019, **9**, 1900039.
- [23] M. Wu, Y. Jing, A. A. Wong, E. M. Fell, S. Jin, Z. Tang, R. G. Gordon and M. J. Aziz, *Chem*, 2020, **6**, 1432-1442.
- [24] S. Guiheneuf, T. Godet-Bar, J. M. Fontmorin, C. Jourdin, D. Floner and F. Geneste, *J. Power Sources*, 2022, **539**, 231600.
- [25] Y. Jing, E. W. Zhao, M.-A. Goulet, M. Bahari, E. M. Fell, S. Jin, A. Davoodi, E. Jónsson, M. Wu, C. P. Grey, R. G. Gordon and M. J. Aziz, *Nat. Chem.*, 2022, **14**, 1103-1109.